,

# Spectral Reflectance Estimation of UAS Multispectral Imagery Using Satellite Cross-Calibration Method

Saket Gowravaram[a], Haiyang Chao[a], Andrew Molthan[b], Tiebiao Zhao[c], Pengzhi Tian[a], Harold Flanagan[a], Lori Schultz[d], and Jordan Bell[b]

[a]*University of Kansas, Lawrence, KS 66045, USA*
[b]*NASA Marshall Space Flight Center, Huntsville, AL 35808, USA*
[c]*University of California, Merced, CA 95343, USA*
[d]*University of Alabama, Huntsville, AL 35487, USA*

**Abstract**

This paper introduces a Satellite-based Cross-Calibration (SCC) method for spectral reflectance estimation of Unmanned Aircraft System (UAS) multispectral imagery. The SCC method provides a low-cost and feasible solution to convert high-resolution UAS images in digital numbers (DN) to reflectance when satellite data is available. The proposed method is evaluated using a multispectral dataset, including orthorectified KHawk UAS DN imagery and Landsat 8 (L8) Operational Land Imager (OLI) Level-2 surface reflectance (SR) data over a forest/grassland area. The estimated UAS reflectance images are compared with NEON Imaging Spectrometer (NIS) SR data for validation. The UAS reflectance showed high similarities with the NIS data for the NIR and Red bands with Pearson's R values being 97% and 95.74% and root mean square errors (RMSE) being 0.0239 and 0.0096 over a 32-subplot hayfield.

*Keywords:* multispectral remote sensing, unmanned aircraft system, satellite remote sensing, cross-calibration, reflectance estimation

## 1. Introduction

Unmanned aircraft systems (UAS) have been widely used for many multispectral remote sensing applications, including tornado damage track identification (Wagner et al., 2019; Gowravaram et al., 2018), agriculture mapping (Torres-Rua et al., 2015; Niu et al., 2019; Zhao et al., 2015), and forest fire monitoring (Ononye et al., 2007; Merino et al., 2012; Fraser et al., 2017). UAS aerial images can facilitate real-time observations for regions of interest at high spatiotemporal resolutions (e.g. sub-meter spatial resolution and hourly temporal resolution), which can enable small-scale feature detection that may or may not be visible in satellite or aircraft imagery. They can also provide data under cloudy conditions when satellite and aircraft imagery are obstructed. However, one of the biggest challenges for UAS based multispectral remote sensing is the retrieval of reflectance from raw orthorectified UAS images in digital numbers (DN).

In recent years, there have been notable contributions towards ground based-radiometric calibration for UAS multispectral imagery (Stark et al., 2016; Edwards et al., 2019). The most popular methods use either commercial or customized ground reflectance target boards as a reference before, during, and after the UAS flight to identify the relationship between DN and reflectance for each spectral band. A semi-automatic-model-based method was proposed to convert raw UAS images to reflectance using a white Barium Sulfate panel and a Halon board (Zaman et al., 2014). Similarly, a customized gray gradient Masonite panel with nine different levels was used for UAS image radiometric calibration using a simplified empirical line method (Wang and Myint, 2015). Their results showed that the relationship between UAS imagery in DN and reflectance is non-linear for many commercial off-the-shelf cameras. Recently, a subband empirical line radiometric calibration method was proposed using a six-band miniature multiple camera array (mini-MCA) by Tetracam (Deng et al., 2018), which used standard diffuse panels as reference boards. The above methods have been widely used in research communities for reflectance estimation of UAS images. However, they are dependent on the accuracy and the Lambertian properties of the reference boards. To avoid this issue, most UAS groups use spectroradiometers before every survey mission to accurately measure the reflectance of the reference boards. These instruments can be expensive and infeasible for many UAS end-users, who are constrained by a budget. Also, many existing UAS data sets have not been converted to spectral reflectance due to a lack of ground spectroscopy measurements.

Satellites have been the primary source for large-scale multispectral remote sensing applications including burn severity mapping, earthquake damage assessment, and landslide extent mapping (Stow et al., 2007; Voigt et al., 2007). Free and open satellite data can be obtained from the National Aeronautics and Space Administration's (NASA) Landsat, Terra, Aqua, and European Space Agency's (ESA) Sentinel. However, these satellites provide imagery at lower spatial resolutions (10 m or lower) with relatively slow revisit times (1 - 16 days).

While satellite imagery possesses reliable radiometric accuracy, UAS can acquire images at desirable spatiotemporal resolutions, which has led to efforts towards understanding the relationship between UAS and satellite remote sensing data. High-resolution aerial observations from UAS were used to increase the spatial resolution of satellite data for precision agriculture (Hassan-Esfahani et al., 2017). Similarly, the variations in Normalized Difference Vegetation Index (NDVI) across different pixel scales were studied among canopy and non-canopy vegetation using various sensing payloads including UAS cameras, Landsat 8 (L8) Operational Land Imager (OLI), and the Moderate Resolution Imaging Spectroradiometer (MODIS) (Wang et al., 2017). Airborne data from manned aircraft has also been explored for multispectral remote sensing (Joan-Cristian et al., 2019). Detailed statistics and cost analysis between UAS, manned air-

craft, and satellite remote sensing platforms were provided for precision viticulture applications (Matese et al., 2015) and a satellite-based local bidirectional reflectance distribution function (BRDF) correction method was introduced for radiometric correction of digital aerial images using data from Landsat 5 and 7 (Tuominen and Pekkarinen, 2004). While satellite, manned aircraft, and UAS all have their advantages and disadvantages, it is important to understand the radiometric relationships between different remote sensing data from various sources for future integrated and improved earth observations.

For accurate integration and comparison of multisource remote sensing data, UAS and satellite reflectance imagery acquired at the same time are preferred to minimize radiometric differences. However, this can be difficult due to other constraints. In such cases, satellite imagery acquired a few days before or after the UAS campaign can be considered for radiometric studies and comparison. For example, UAS and RapidEye images three days apart were used for precision viticulture applications (Matese et al., 2015), and L8 images acquired two days after a UAS mission were compared to the UAS reflectance and NDVI values for vegetation monitoring (Berra et al., 2017). Similarly, an adaptive classification approach for precision agriculture monitoring was developed where drone and L8 images acquired 7 days apart were used (Murugan et al., 2017).

This paper focuses on the development of a low-cost cross-calibration method for estimation of UAS spectral reflectance at high spatial resolution using satellite reflectance data of the same area which can be beneficial to UAS operators and research groups who want to: 1) collect new UAS data but do not possess accurate spectroradiometers and ground target boards, 2) calibrate existing UAS data collected without a ground reflectance reference, and 3) study the radiometric relationships between multi-scale remote sensing data from satellite, manned aircraft, and UAS for enhanced Earth observations. The proposed method is demonstrated using orthorectified KHawk UAS DN imagery and L8 OLI Level-2 (L2) surface reflectance (SR) data of a forest/grassland area in Kansas. The cross-calibration functions between these two data are first identified for each spectral band and then used to convert high-resolution UAS DN images to reflectance. The proposed Satellite-based Cross-Calibration (SCC) method is finally validated by comparing the estimated UAS reflectance images with National Ecological Observatory Network (NEON) Image spectrometer (NIS) atmospherically corrected SR data.

## 2. UAS and Satellite Remote Sensing Data

This section provides descriptions of the study area and the remote sensing data used to formulate and validate the proposed method.

### 2.1. Study Area

An area of 0.5 square kilometers at the University of Kansas Field Station (KUFS) is selected as the study area (Fig. 1). It is located at $39.054°, -95.190°$, elevation 331 m in the deciduous forest and tall grass prairie ecotone of northeastern Kansas (KBS, 2019). Fig. 1 shows the the study area and the corresponding orthorectified UAS image. Note that this area contains a 32-subplot hayfield (labelled in Fig. 1) close to the northwest boundary, which is maintained annually by the Kansas Biological Survey (KBS). Each subplot (10 m × 10 m) is given the same treatment (seeded, fertilized, or hayed) and is maintained to have the same vegetation (Foster et al., 2010). This hayfield is well suited for validation of the proposed SCC method. This area is also one of the 81 NEON field sites, a 30-year ecological monitoring project, and one of the most extensive initiatives of the National Science Foundation (NSF) (NEON, 2019).
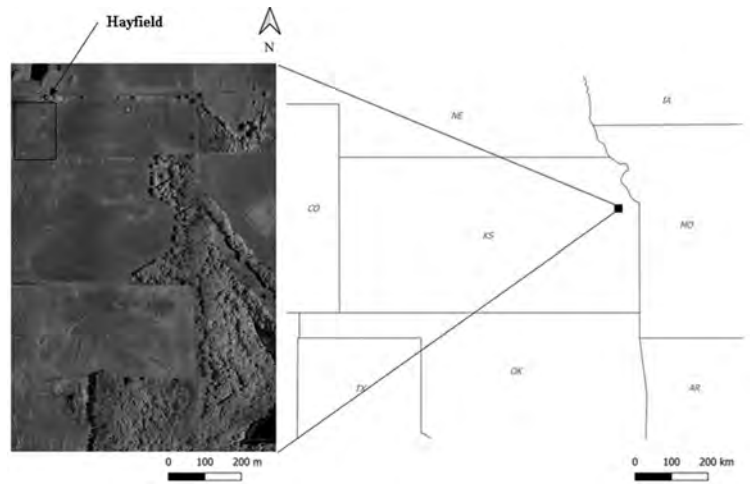
Figure 1: Study area.

## 2.2. KHawk UAS Data

KHawk 2 UAS is a low-cost multispectral remote sensing platform developed by the Co-operative Unmanned Systems Lab (CUSL) at the University of Kansas, shown in Fig. 2. It is equipped with a Ublox-Lea 6h GPS receiver and a Paparazzi TWOG autopilot, which can support both manual and autonomous flight. The detailed specifications are provided in Table 1. The UAS can carry one camera at a time for image acquisition. In this paper, two PeauPro82 modified GoPro Hero 4 Black cameras (PeauProductions, 2017) are used for multispectral image acquisition with one providing imagery in the visible spectrum (RGB) and the other in the NIR spectrum. The spectral characteristics of the modified GoPro camera are shown in this section.

Table 1: KHawk 2 UAS specifications

| Description | Value |
|---|---|
| Take-off Weight | 1.7 kg |
| Wingspan | 1.2 m |
| Cruise Speed | 16 m/s |
| Endurance | 30 min |
| Spatial Resolution (at 120 m above the ground) | 0.1 m |

The KHawk 2 UAS was deployed for multispectral data acquisition over the study area on June 7, 2017. Two flights were conducted, one for NIR (09:49-10:19 AM) and the other for RGB (12:11-12:32 PM) video acquisition. It was flown autonomously at an altitude of 120 m above ground level with a minimum horizontal and vertical overlapping percentage of 75% between flight lines to ensure accurate image orthorectification. The KHawk 2 flight locations (white circles) which are used for the orthorectification are shown in Fig. 2. The acquired images were georeferenced and orthorectified using Agisoft Photoscan Professional software to produce orthomosaics in visible and NIR bands at a spatial resolution of 0.1 m. The spatial accuracy of the generated orthomosiacs was calculated by performing a comprehensive comparison with

4

ArcGIS World Image which has a spatial resolution of 0.5 m or better in the continental United States (ArcGIS, 2021). A total of 10 high-quality control point pairs were randomly selected from the UAS and ArcGIS World images for comparison. The horizontal root mean square error (RMSE) for these 10 points is 4.72 m.
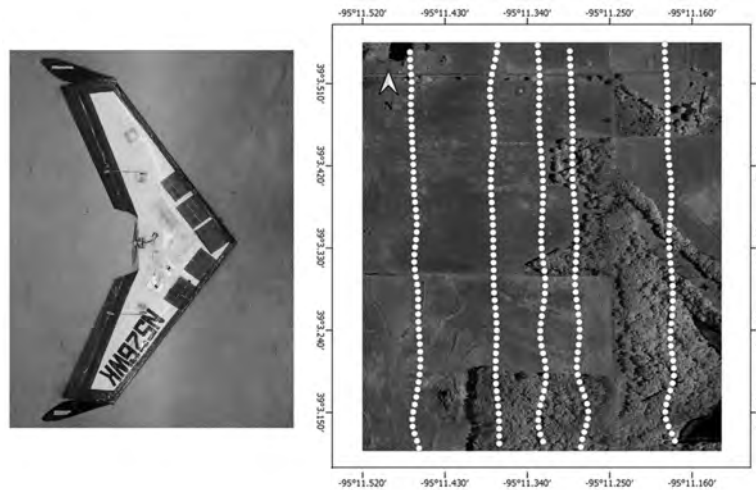


Figure 2: KHawk 2 UAS (L) and KHawk 2 UAS flight path over the study area (R).

Table 2: Spectral Characteristics of KHawk 2 and L8 Remote Sensing Systems

| Sensor | Bands | FWHM (nm) | Peak (nm) |
|---|---|---|---|
| OLI | Red | 635.85–673.32 | 654.59 |
| | NIR | 850.54–878.79 | 864.67 |
| Modified PeauPro 82 GoPro (RGBt) | Red | 583.9–710 | 627.6 |
| Modified PeauPro 82 GoPro (NIR) | NIR | 825.4–880 | 852.7 |

### 2.3. Landsat 8 Satellite Data

The L8 satellite is equipped with OLI and Thermal Infrared Sensor (TIRS) instruments for multispectral image acquisition. The OLI measures light at 9 spectral bands ranging from 430 to 1380 nm (NASA, 2019) . Operating at an altitude of 705 km above ground level, the OLI can provide calibrated reflectance images of the Earth every 16 days at spatial resolutions of 15 m (panchromatic band) and 30 m (all other bands). In this paper, OLI L2 SR images of the study area acquired on June 7, 2017 at 12:00 PM are used. The OLI L2 SR images are derived through the atmospheric correction of OLI Level-1 (L1) products using the Landsat Surface Reflectance Code (LaSRC) algorithm (USGS, 2020). The L8 OLI images demonstrate a spatial accuracy of 12 m or better (NASA, 2021).

The KHawk GoPro and OLI sensor spectral characteristics (PeauProductions, 2017) are compared and shown in Table 2. It can be observed that the NIR band of OLI is similar to the GoPro camera while the Red band of OLI is narrower than that of the GoPro camera.

## 3. Spectral Reflectance Estimation of UAS Imagery

This section provides detailed descriptions of the proposed method for spectral reflectance estimation of multispectral UAS DN imagery. The objective of this method is to convert raw UAS images in DN at high spatial resolution to reflectance using available satellite reflectance data. The main advantage of this method is that spectral reflectance can be estimated from UAS DN images for free or at very low-cost. In addition, this method will ensure similarity between the UAS and satellite imagery, which can later be used for multi-scale remote sensing applications of large fields such as crop monitoring and disaster assessment. The proposed method can be broken into the following steps for researchers who want to collect new UAS data.

1. UAS Campaign Planning - Plan the UAS data acquisition based on the availability of satellite data and favorable weather conditions. UAS campaign should follow the time schedule of satellite imagery collection.
2. UAS Data Processing - Collect UAS multispectral imagery of a given region of interest and perform georeferencing and orthorectification.
3. Satellite Data Acquisition - Satellite reflectance data of the region of interest is recommended to be acquired based on certain factors including acquisition time, cloud cover, and atmospheric correction (explained in further detail in Sec. 3.1).
4. Cross-Calibration and Conversion - After the acquisition of UAS DN and satellite reflectance imagery, the SCC method can be implemented to identify the cross-calibration functions for each spectral band (explained in further detail in Sec. 3.2). The identified cross-calibration functions can then be used to convert raw UAS DN imagery to reflectance values.

For researchers who have already collected their raw UAS data without ground calibration boards or ground spectrometer measurements, the following steps can be used instead.

1. Find suitable reference of surface reflectance either from satellites (L8, Sentinel 2, Planet, etc.) or from airborne data (NAIP, NEON, etc.).
2. UAS Data Processing – (same as above).
3. Cross-Calibration and Conversion – (same as above).

### 3.1. Satellite Data Acquisition

Satellite reflectance data for a given region of interest (UAS survey area) can be downloaded for free or at low-cost from designated websites such as United States Geological Survey (USGS) Earth Explorer, Copernicus Open Access hub, Planet, etc. Reflectance data from any satellite (Landsat, Sentinel, Planet, etc) can be used in this method and the following factors need to be considered during the selection.

1. Acquisition Time: The satellite data acquisition time can be a critical factor in the effectiveness of the method. It is desired that the satellite data is acquired at the same time as that of the UAS image so that the reflectance is the same. In case of unavailability of such data, satellite data acquired close to the time of UAS campaign can be potentially used.

2. Cloud Cover: Ideally, cloud free satellite observations of the region of interest are desired. In cases with partial cloud obstruction, the unobstructed areas can be used to identify the cross-calibration functions which can then be used to calibrate the UAS data in cloud-obstructed areas. If there is a total cloud obstruction, satellite images acquired before or after the UAS survey can be used if available.

3. Atmospheric Correction: Satellite images are required to be atmospherically-corrected to convert UAS DN to surface reflectance. Therefore, L2 data is recommended.

Satellite images acquired at the same time with UAS are preferred for this method. In cases when no suitable satellite images are available, aircraft imagery such as those from National Agriculture Imagery Program (NAIP) or NEON can also be used to serve as a reference reflectance image of the same area. The SCC method is described in the following subsection.

## 3.2. Satellite-based Cross-Calibration Method

Given an orthorectified UAS image $X'$ in DN at high spatial resolution ($kM \times kN$ pix.) and a satellite atmospherically-corrected reflectance image $Y$ at medium spatial resolution ($M \times N$ pix.), a cross-calibration function $F(X')$ can be identified for each spectral band that can convert UAS images in DN at high spatial resolution to spectral reflectance. Here, $k$ is the ratio between the spatial resolutions of satellite and UAS images which can be derived from the dataset. For example, $k$ is 30 if the spatial resolutions of satellite and UAS images are 30 m and 1 m respectively. The main steps of this method (Fig. 3) include:

1. UAS image resampling: Resample the high-resolution UAS image ($X'$) to a medium-resolution image ($X$) to match the spatial resolution of the satellite image ($Y$). Existing methods like nearest neighbor, bilinear, or bicubic methods can be used. Bicubic interpolation is used in this work.

2. Pixel selection: Select UAS and satellite pixel pairs at medium spatial resolution, ($X_1, Y_1$), which is a subset of the original UAS and satellite image pair, ($X, Y$). Here, the objective is to exclude pixels that can potentially induce errors in the function identification and is explained in detail later in Sec. 3.2.1.

3. Function identification: Use least-squares optimization methods to find the optimal cross-calibration function based on selected pixel pairs.

4. UAS reflectance estimation: Apply the identified function to the high-resolution UAS DN image ($X'$) and finally obtain UAS reflectance image ($Y'$).

## 3.2.1. Pixel Selection

In this work, the pixel pairs are selected based on two conditions, a) low sub-pixel variability and b) non-shadow pixels.

The first condition is to exclude pixels with high sub-pixel variability within a medium-resolution pixel (e.g. a 30 m × 30 m area for one OLI pixel). This is an important step as it can reduce the impact of mixed pixel effect of the lower resolution satellite image on the overall method. Essentially, this condition filters out the pixels that correspond to areas with varying reflectance values. This is determined based on the sub-pixel Coefficient of Variation ($CV$), calculated from high spatial resolution UAS image in DN. CV is the standard deviation divided by the mean value ($\sigma/\mu$) within a pixel at medium-resolution. The concept is further shown in Fig. 4. $CV_B$ represents the CV of pixel $B$ in $X$, which is calculated using the mean ($\mu_A$) and standard deviation ($\sigma_A$) of all the pixels in a subgroup $A(k \times k$ in $X')$. A threshold can be
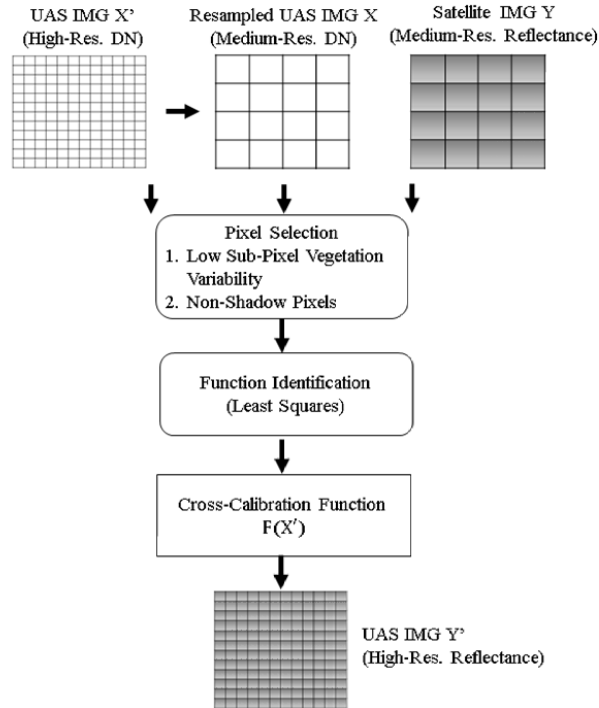
Figure 3: SCC method flowchart.

empirically defined to exclude all pixels in $X$ with higher CV. The recommended threshold can be selected as the mean CV of all the pixels in the image, $\bar{CV}$.

The second condition aims to exclude all the shadow pixels. Generally, UAS images acquired at low altitudes tend to capture leaf canopy shadows. Since these shadows may not be observed in fine detail from satellite images due to lower spatial resolutions and may also show different patterns due to different acquisition time and different viewing angles/distance, it is not recommended to include the shadow regions for function identification. An empirical pixel thresholding method can be used to detect shadows in the UAS images, where thresholds can be applied to identify all the shadow pixels (Aboutalebi et al., 2019). It is worth mentioning that there exist other feature-based image processing methods for shadow detection which can also satisfy this condition. After detection of the shadow pixels in high-resolution UAS imagery, the corresponding pixels in resampled UAS imagery at medium-resolution can then be rejected.

In summary, the low sub-pixel variability condition can be first applied to the UAS image, $X$, which rejects pixels exhibiting high sub-pixel variability ($CV \geq \bar{CV}$). This condition detects and rejects many shadow pixels as long as the shadows occupy only a portion of the pixel. However, in cases where pixels are mostly covered with shadows, the second condition is needed.
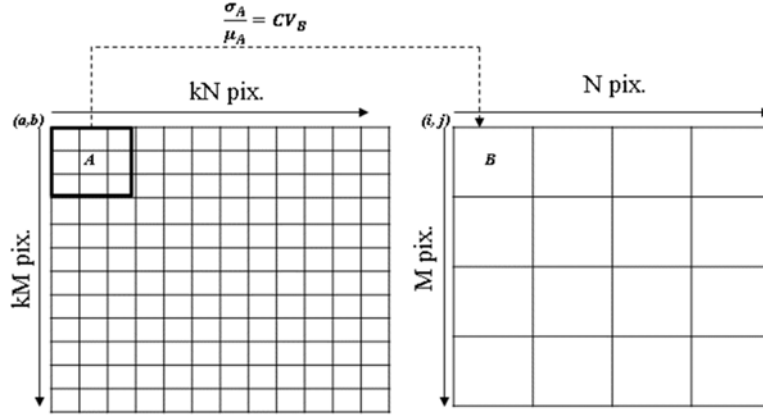
Figure 4: Coefficient of variation calculation using images $X'$ (L) and $X$ (R).

### 3.2.2. Function Identification

The objective of this step is to identify the cross-calibration functions between the selected sample, $(X_1, Y_1)$. Both linear and nonlinear functions have been used in the literature to convert DN to reflectance. In this paper, the exponential function is selected based on recent literature (Wang and Myint, 2015; Deng et al., 2018) using similar cameras (commercial grade). The Ordinary Least Squares (OLS) and Weighted Least Squares (WLS) regression methods are used for the parameter identification of the optimal cross-calibration functions.

*Ordinary Least Squares.* The OLS method is used to estimate the unknown parameters in a linear regression model by minimizing the sum of squared errors. It is worth emphasizing that, the OLS method is optimal under the assumption that the errors or the residuals are homoscedastic and serially uncorrelated across the measurement range (StatisticsSolutions, 2020). For remote sensing images from different sources and at varying spatial resolutions, there is a high possibility of outliers and changing uncertainties across the reflectance range which may violate this condition.

*Weighted Least Squares.* When the OLS assumption of constant variance in the errors is violated (not homoscedastic), the WLS method can be used. The main difference is that in WLS, each data point in the given set of observations is weighed differently based on their resulting error variance. For example, data points with high error variances (e.g. outliers) are weighed very low compared to points with lower error variances. As a result, the WLS method is less sensitive to outliers as compared to the OLS method and has been used in remote sensing (Zhang et al., 2008; Shimabukuro and Smith, 1991; Nencini et al., 2008). Another difference is that the WLS minimizes the sum of weighted squared error instead of sum of squared error as shown below (Mathworks, 2020).

$$S = \sum_{i=1}^{n} w_i (y_i - \hat{y}_i)^2, \tag{1}$$

where $w_i$ are the weights of each data point.

9

In this paper, a variant of the WLS, called the Iteratively Weighted Least Square Regression (IWLSR) is used. This method has been successfully implemented for automatic relative radiometric normalization of satellite imagery (Zhang et al., 2008). The IWLSR method, initialized with the error residuals from the OLS method, iteratively determines the optimal weights for each data point in the given set of observations. The method is described below (Zhang et al., 2008).

Consider a set of observation data, $(x_j, y_j)$ such that $j = 1, 2, 3....n$. The OLS is first used to estimate the slope and intercept, $m$ and $p$ respectively, such that:

$$y_j = mx_j + p + \epsilon_j, \tag{2}$$

where $\epsilon_j$ is the error residual for the $j$th data point. Next, a variable $t$ is defined such that $t = \epsilon/\sigma_\epsilon$, where $\sigma_\epsilon$ is the standard deviation of the error residual vector. Here, $t$ is an approximate one degree of freedom chi-square distribution ($\chi^2(1)$). This is used to calculate the weight vector, $w$, for the next iteration.

$$w = P\{\chi^2(1) > t\} = 1 - P\{\chi^2(1) \le t\}. \tag{3}$$

$P$ in the above equation represents the chi-squared cumulative probability function. The above steps constitute one iteration. With the new weights, the updated slope and intercept are calculated, which starts the next iteration. The algorithm runs until the difference in the weights between two consecutive iterations falls below a specified value.

Finally, cross-calibration functions are identified for each spectral band that can be used to estimate spectral reflectance of UAS DN images. The SCC method is demonstrated in the next section.

## 4. Results

The results of the proposed SCC method is presented in this section using a multispectral data set including KHawk UAS DN images and OLI SR data. The estimated KHawk high-resolution reflectance images are compared with high-resolution NIS SR images for validation.

### 4.1. Reflectance Estimation of KHawk UAS DN Images

The multispectral dataset is shown in Fig. 5, including orthorectified high-resolution (1 m) KHawk DN, resampled medium-resolution (30 m) KHawk DN, and medium-resolution (30 m) OLI SR images for the NIR band. The high-resolution and the resampled medium-resolution KHawk DN images share the same pixel range of 100-200 and the OLI SR image ranges from 0-0.6.

Pixel pairs are selected using the Pixel Selection method described in Sec. 3.1. In this paper, the mean CV in the image $X$, $\bar{CV}$ is used as the threshold to perform this selection. Fig. 6 shows the selected pixels (circles) overlaid on the orthorectified and resampled UAS NIR DN image. As mentioned, the excluded pixels either represent high sub-pixel variability or shadows (example shown in Fig. 6).

OLS and WLS regression methods are tested on the selected pixel pairs for function identification. Fig. 7 shows the identified exponential cross-calibration functions using both methods for the NIR and Red bands. Note that exponential functions can be converted to linear functions by taking the natural log on both sides of the equation.
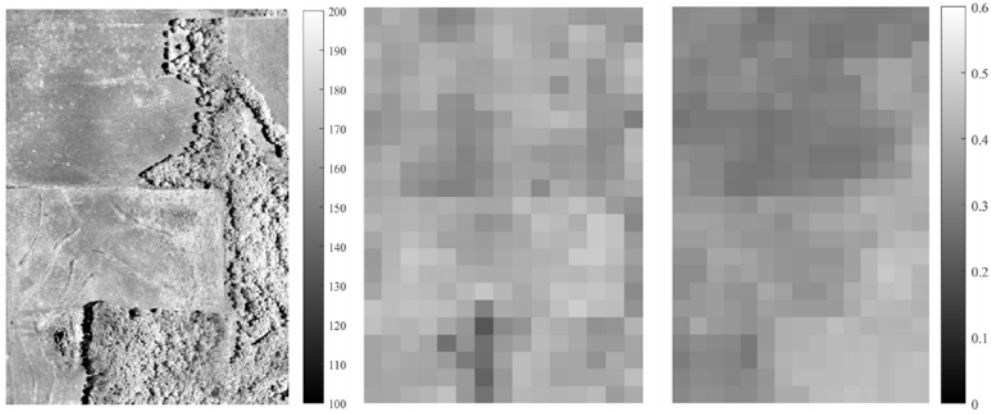
Figure 5: KHawk UAS and OLI NIR images of study area: orthorectifed high-resolution KHawk DN image (L), resampled medium-resolution KHawk DN image (M), and medium-resolution OLI SR image (R).



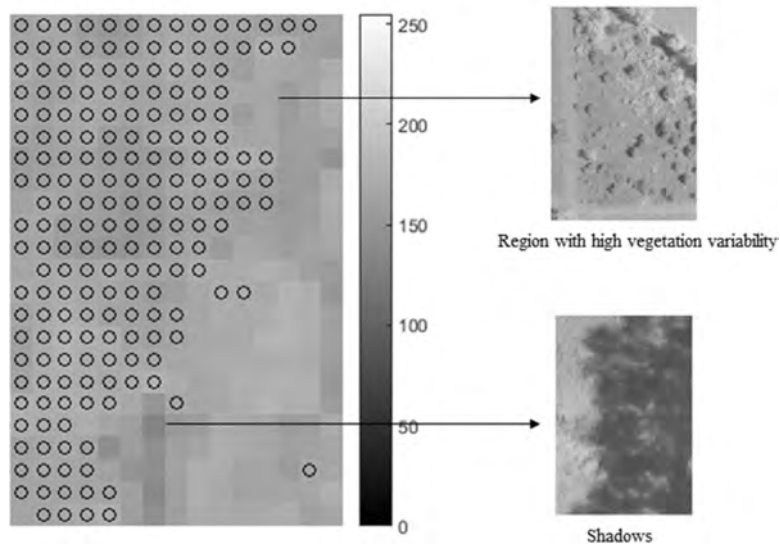Region with high vegetation variability

Shadows

Figure 6: Selected sample pixels after Pixel Selection and example of excluded pixels.

In order to identify the optimal exponential function from the aforementioned regression methods, error residuals and error variances are analyzed. Fig. 8 shows the error residual plot for both methods, where the y-axis represents the error residual and x-axis ($y_{hat}$) represents the natural log of the estimated KHawk reflectance. It can be observed that the WLS method results in smaller and more importantly, more consistent error variance as compared to OLS. The total error variance for NIR/Red bands were 0.0061/0.0156 and 0.0011/0.0025 for the OLS and WLS methods respectively. Therefore, the WLS method is selected for function identification. Table 3 shows the functions identified using the OLS and WLS methods. Here, $x_i$ represents the KHawk DN values and $y_i$ represents the OLI SR values with $i = 1, 2, 3, ...N$, where $N$ is the
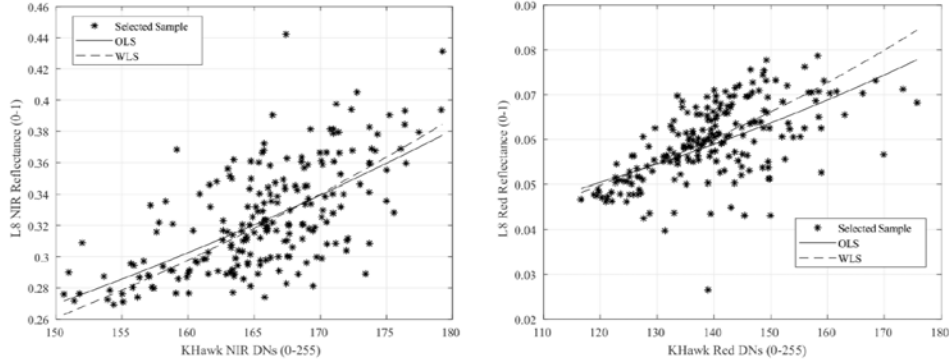
11

Figure 7: Identified cross-calibration function curves overlaid on selected sample for NIR (L) and Red (R) bands.

total number of pixels in the selected pixel pairs. The identified functions are used to convert the high-resolution KHawk DN images to spectral reflectance for the NIR and Red bands.
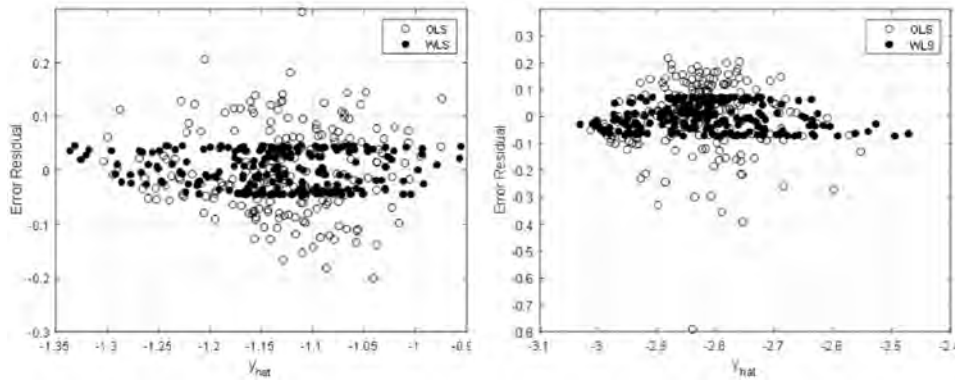


Figure 8: Error residuals for NIR (L) and Red (R) bands.

Table 3: Identified functions using the OLS and WLS methods.

| Band | OLS | WLS |
|------|-----|-----|
| NIR | $y_i = 0.0483e^{0.0115x_i}$ | $y_i = 0.0358e^{0.0132x_i}$ |
| Red | $y_i = 0.0198e^{0.00078x_i}$ | $y_i = 0.0160e^{0.00095x_i}$ |

## 4.2. Validation Using NIS Images

The estimated KHawk reflectance images at 1 m spatial resolution are compared to NIS SR images at the same resolution for validation. This subsection is broken down into: 1) NEON data description, 2) effects of spectral and spatial resolution on reflectance, and 3) NIS and KHawk reflectance comparison.

### 4.2.1. NEON Data Description

NEON is a continental-scale ecological observation facility project funded by NSF and operated by Battelle Memorial Institute (NEON, 2019). NEON provides calibrated terrestrial, aquatic, atmospheric, and remote sensing data of 81 field sites across the United States to the scientific community, including the study area used in this paper. The NEON aircraft is installed with a push broom collection style NIS, which was designed and built by NASA's Jet Propulsion Laboratory (JPL) for hyperspectral remote sensing. The NIS measures light at 426 spectral bands (with 5 nm spectral resolution) ranging from 380 to 2500 nm and produces orthorectified reflectance mosaics at a spatial resolution of 1 m (NEON, 2020). The aircraft is flown once each year over the study area at an altitude of 1000 m above ground level. The orthorectified images used in this paper correspond to a flyby on June 9, 2017 at 3:38 PM. Note that these images are atmospherically corrected using the ATCOR-4 algorithm.

### 4.2.2. Effect of Spectral and Spatial Resolutions on Reflectance

Difference in spectral and spatial resolutions can have an effect on the changes in reflectance between images from different remote sensing platforms. In order to use high-resolution NIS images for validation, consistency in reflectance between NIS and OLI SR images needs to be established.

NIS is a hyperspectral instrument and has a higher spectral resolution (narrower wavelength range) than the OLI. This can cause some inconsistencies between the reflectance images from both instruments. In order to minimize these differences, spectral convolution on the hyperspectral data can be performed to match the spectral response of the multispectral sensor (Zhao et al., 2010; Jarecke et al., 2001; Barry et al., 2002). In this paper, a weighted-sum based spectral convolution method is used, where the spectral resolution of the hyperspectral data is transformed to a lower value (Badawi et al., 2019; Meyer and Chander, 2007). The weights are determined using the OLI prelaunch Relative Spectral Response (RSR) for the NIR and Red bands (NASA, 2020). The equation used to perform the convolution is shown below:

$$\rho_i = \frac{\int_{\lambda_1}^{\lambda_2} \rho_0(\lambda) \; RSR_i(\lambda) \; d\lambda}{\int_{\lambda_1}^{\lambda_2} \; RSR_i(\lambda) \; d\lambda}, \tag{4}$$

where $\rho_i$ is the spectrally convoluted NIS SR corresponding to band $i$, $\rho_0(\lambda)$ and $RSR_i(\lambda)$ are the NIS SR and the OLI spectral response of wavelength $\lambda$ in band $i$ respectively, $\lambda_1$ and $\lambda_2$ are the lower and upper wavelengths of the OLI spectral range for band $i$.

In addition to spectral resolution differences, which is an instrument-dependent factor, differences in spatial resolution (study area-dependent) can also cause reflectance inconsistencies between images from different platforms. Goetz (1997) observed that images of uniform grasslands show consistency across different spatial resolutions. Similar patterns have also been observed in open grasslands with varying grass species (Liu et al., 2017). Given these findings, the grass regions of the study area are expected to be consistent across different spatial resolutions. However, the tree regions may show differences due to factors such as canopy shadows and inter tree spacing, which are generally observed in finer detail in high-resolution images.

The rest of this subsection is focused on analyzing the effect of spectral and spatial resolutions on reflectance for the study area, including, 1) spectral resolution effect: comparison between resampled NIS and OLI images at 30 m resolution and 2) spatial resolution effect: comparison between high-resolution (1 m) and resampled medium-resolution NIS images (30 m) for the

grass and tree regions. The high-resolution NIS and medium-resolution OLI NIR images are shown in Fig. 9.
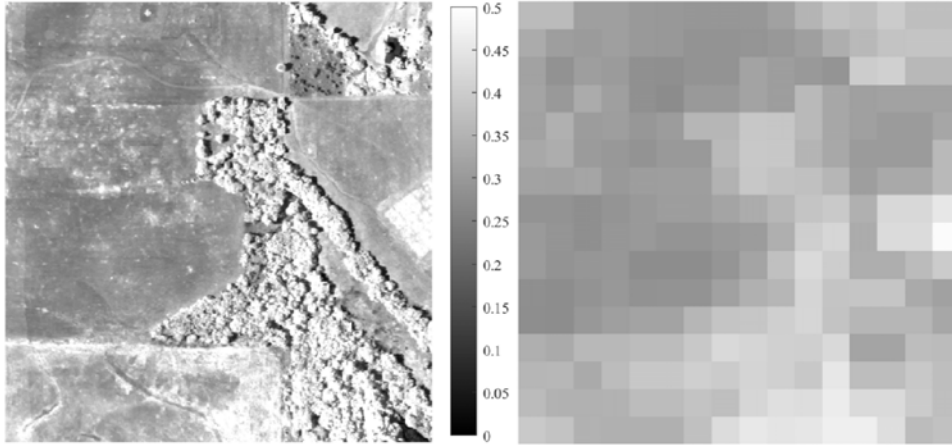


Figure 9: High-resolution NIS (L) and medium-resolution OLI NIR (R) images of study area.

*Effect of Spectral Resolution.* Although the NIS images are spectrally convoluted using Eq. 4, some differences are still expected. The NIS NIR and Red SR images are resampled to 30 m resolution and compared to corresponding OLI images, shown in Fig. 10. It can be observed that while the NIR band shows high similarities for most of the points, a constant bias is seen in the Red band. The RMSE and mean percentage (MP) of the difference between images from the two sources are calculated for each band to be 0.0112 and $-0.0043$ for the NIR band and 0.0014 and $-0.0274$ for the Red band.
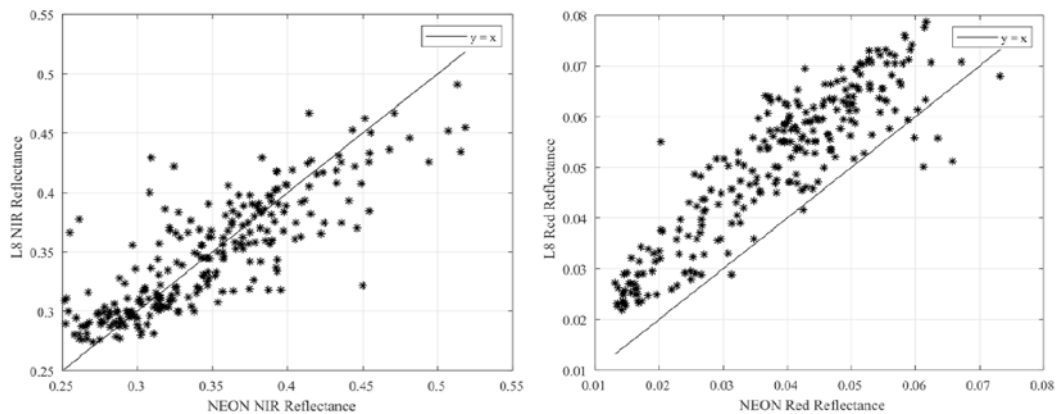


Figure 10: NIS and OLI SR comparisons for the NIR (L) and Red (R) bands.

*Effect of Spatial Resolution.* The differences between the high-resolution (original) and resampled NIS images are calculated for the grass and tree areas separately. One pixel in the resampled

NIS image is compared to the mean of the corresponding $30 \times 30$ pix. grid in the high-resolution NIS image. RMSE and mean percentage error (MPE) are calculated for each band and shown in Table 4. Additionally, sub-pixel variability within each $30 \times 30$ pix is also calculated using the CV. Mean CVs for grass and tree areas are also shown in Table 4.

Table 4: Effect of spatial resolution on reflectance in grass and tree areas.

| Region | Mean CV (%) | | RMSE | | MPE (%) | |
|---|---|---|---|---|---|---|
| | NIR | Red | NIR | Red | NIR | Red |
| Grass | 11.01% | 17.17% | 0.028 | 0.0073 | 0.1% | 2.4% |
| Tree | 30.85% | 44.97% | 0.040 | 0.0068 | 2.8% | 8.8% |

It can be observed that the grass areas show higher consistencies and lower CV than the trees. The change of spatial resolution has a small impact on the reflectance in grass areas, which also provides a justification for our proposed cross-calibration method.

*4.2.3. NIS and KHawk Reflectance Comparison*

The estimated KHawk spectral reflectance images at 1 m spatial resolution are compared with NIS SR in detail in this section. First, the KHawk images are registered with the NIS images using a point mapping technique in MATLAB (MATLAB, 2020). This step is necessary to reduce errors due to misalignment between the two images. A projective transformation is performed on the KHawk image using 12 selected control point pairs. The registered NIR and Red reflectance images from both platforms are shown in Fig. 11. Note that the black holes in the NIS images (close to the left boundary) and in the KHawk Red image (right boundary) are caused by orthorectification and are not used for comparison. Two analyses are performed for comparison, 1) using a 32-subplot hayfield close to the northwest boundary and 2) using selected grass and tree regions.

*Hayfield Comparison.* The 32-subplot hayfield serves as a good reference for comparison because, 1) the area is observed in images from both platforms and each subplot (grid size 10 m × 10 m) is distinguishable, 2) the area is treated annually by KBS and the same treatment is given within each subplot, ensuring that the reflectance within each subplot is similar (Foster et al., 2010). Fig. 12 shows the hayfield observed by the NIS (L) and KHawk (R) NIR images. The black box in each subplot represent a 6 m × 6 m window. All pixels within the window are averaged to produce one value per subplot.

The averaged KHawk and NIS SR values for each subplot are compared in Fig. 13. A good agreement can be observed between both images for the NIR and Red bands with high correlations of 97% and 95.74% and low RMSE of 0.0239 and 0.0096.

*Selected Region Comparison.* In addition to the hayfield analysis, other regions in the area are also selected for NIS and KHawk comparison. It is worth mentioning that comparing all the pixels between the two images is difficult here due to pixel alignment and georeferencing uncertainties. In fact, KHawk orthorectified images are generated from many images and has a RMSE error of 4.72 m. Alternatively, six 3 m × 3 m regions are manually selected for comparison, including, three grass regions and three tree regions, shown in Fig. 14-15. The region size (3 m × 3 m) is selected based on the average tree canopy size observed in this data set. Note that shadows are excluded from the selected regions for a fair comparison. The six NIS and KHawk
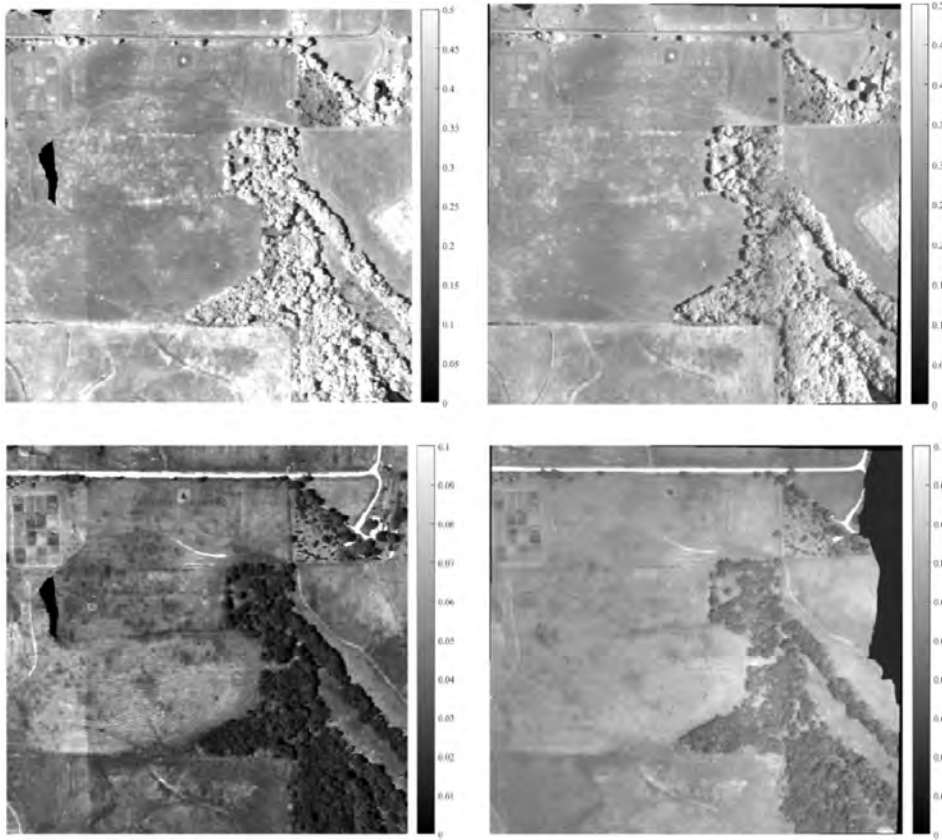
Figure 11: NIS (L) and KHawk (R) spectral reflectance images in NIR (top) and Red (bottom) bands.

reflectance values and differences between them are shown in Fig. 16 and Table 5 respectively. Mean absolute error (MAE) and RMSE were found to be 0.0243 and 0.0306 for the NIR band, and 0.0178 and 0.0163 for the Red band.

Two trends can be observed from Table 5, 1) tree regions exhibit higher differences in both NIR and Red bands, 2) Red band shows slightly higher differences across most of the regions. These observations are similar to those found in Sec. 4.2.2.

In summary, the estimated KHawk reflectance images showed high similarities with the NIS images in grass regions, and slightly lower similarities in the tree regions. This shows the potential of the proposed SCC method for other similar fields (e.g., dominant grassland), given the availability of an atmospherically corrected satellite reflectance image.

## 5. Discussions

The SCC method presented in this work provides an effective and low-cost solution for the spectral reflectance estimation of UAS DN images, under the assumption that there exists satellite SR data of the same area around the same time. The main advantage of this method is that UAS images can be converted to reflectance images without using ground reflectance target
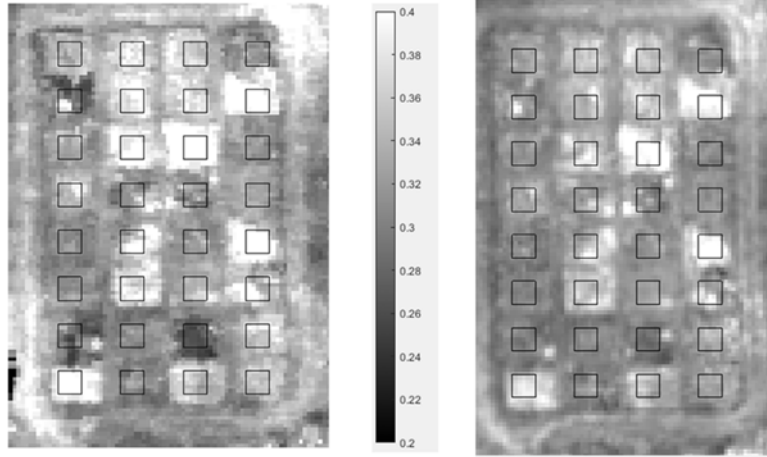
16

Figure 12: Hayfield in NIS (L) and KHawk (R) NIR reflectance images (6 m × 6 m for each box).
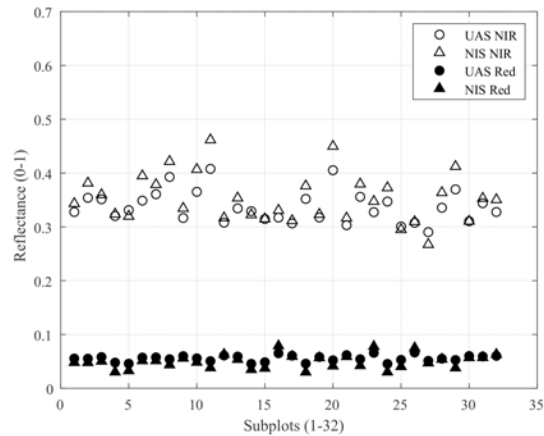


Figure 13: NIS and KHawk reflectance values of the 32-subplot hayfield.

boards and expensive spectroradiometers. Apart from its contributions to the UAS community, the SCC method can also greatly benefit the satellite remote sensing community by establishing cross-calibration functions between UAS and satellites thus enabling future development of multisource and multiscale data fusion such as super-resolution for satellite imagery.

Since the proposed method uses images from different instruments, co-registration accuracy, differences in spectral resolution (Teillet et al., 1997) and conditions during data acquisition between UAS and satellite images can play a vital role in the accuracy of the function identification. Performing an accurate co-registration analysis between UAS and satellite images can be a challenging task considering the differences in their spatial resolutions (0.1 m and 30 m respectively). However, since the spatial accuracy of the KHawk (4.72 m or better) and L8 OLI (12 m or better) images are smaller than the pixel size of the L8 OLI image, the impact of co-registration accuracy on the identified functions are not expected to be substantial. In this paper, images from three
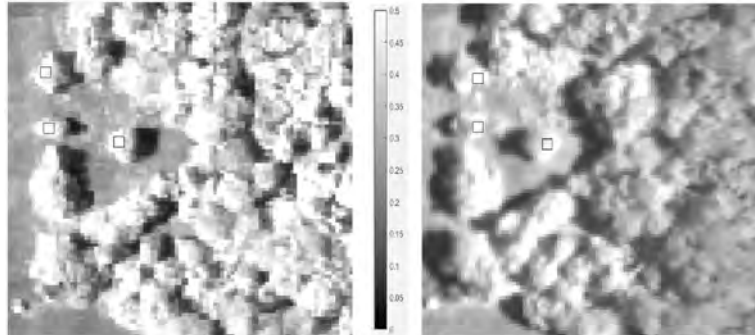
17

Figure 14: Selected tree regions in NIS (L) and KHawk (R) NIR reflectance images (3 m × 3 m for each box).
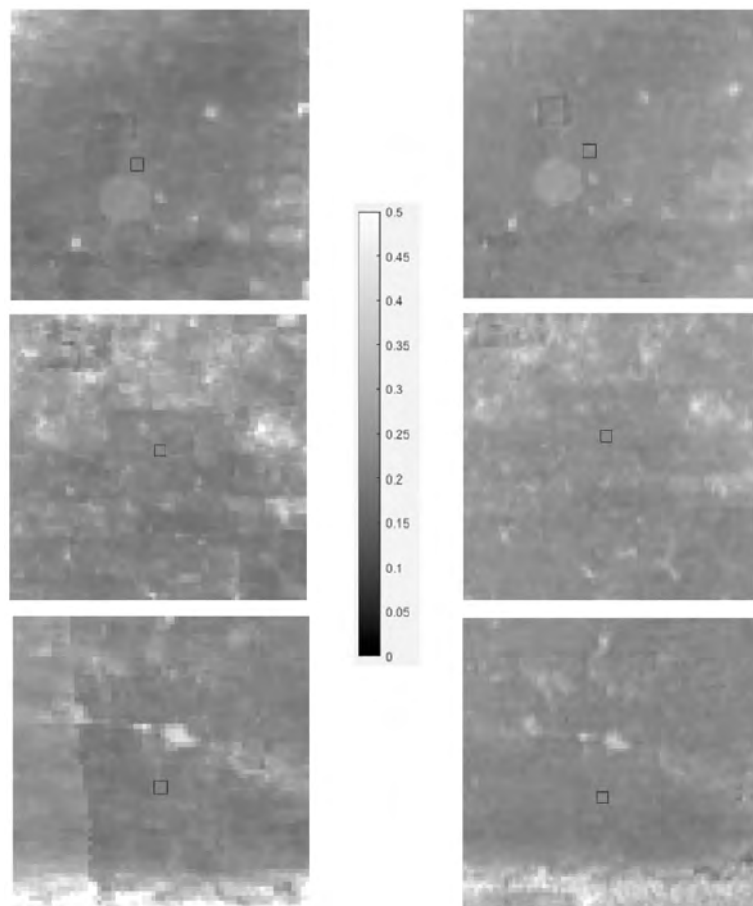


Figure 15: Selected grass regions in NIS (L) and KHawk (R) NIR reflectance images (3 m × 3 m for each box).
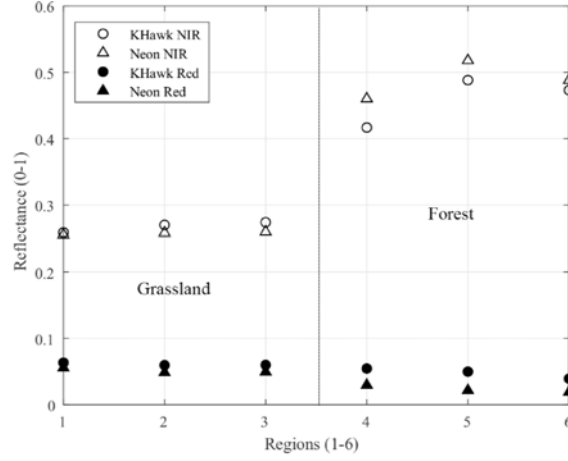
Figure 16: NIS and KHawk reflectance values of the selected regions.

Table 5: Reflectance differences between NIS and KHawk.

| Region | NIR | | | Red | | |
|--------|------|-------|------------|------|-------|------------|
|        | NIS  | KHawk | Difference | NIS  | KHawk | Difference |
| Grass  | 0.2581 | 0.2595 | 0.0014 | 0.0577 | 0.0658 | 0.0082 |
| Grass  | 0.2599 | 0.2736 | 0.0137 | 0.0487 | 0.0583 | 0.0096 |
| Grass  | 0.2706 | 0.2787 | 0.0081 | 0.0501 | 0.0601 | 0.0100 |
| Tree   | 0.4957 | 0.5454 | 0.0497 | 0.0343 | 0.0547 | 0.0204 |
| Tree   | 0.5235 | 0.4762 | -0.0473 | 0.0224 | 0.0476 | 0.0251 |
| Tree   | 0.4860 | 0.5118 | 0.0258 | 0.0229 | 0.0473 | 0.0244 |

sensors are used, namely, KHawk 2 UAS GoPro, OLI, and NIS. Table 2 shows that the spectral characteristics between the GoPro and OLI sensors have small differences in peak wavelength (< 27 nm) for both bands (Table 2). The NIS SR data is spectrally convoluted to match the spectral response of the OLI sensor using (4). It can be observed from Fig. 10 that although the NIR images from the NIS and OLI sensors show high similarities, the Red images have some differences. Similar trends were also observed in Badawi et al. (2019), where the visible band images between NIS and OLI showed lower similarities. Additionally, the OLI and NIS SR data are subject to uncertainties of $5 - 10\%$ respectively (Badawi et al., 2019), which can also cause differences between their respective SR images.

Conditions such as sun angle, clouds, and weather can also affect the accuracy of the proposed method. The ideal case is when the satellite and UAS images are acquired at the same time under similar weather conditions. However, due to practical issues, images acquired a few days apart are also acceptable, especially during the growing season (Apr.-Sept.), when the weather conditions are similar. The KHawk and OLI images used in this paper were acquired on the same day (June 7, 2017) with the KHawk NIR and RGB images acquired during 09:49-10:19 AM and 12:11-12:32 PM respectively, and the OLI images at 12:00 PM. The NIS image was acquired two days later, on June 9, 2017 at 03:38 PM. It can be observed from Fig. 14 that leaf canopy shadows are observed in opposite directions in NIS (towards east) and UAS (towards

west) images. While the effect of shadows on the grass areas is not significant, more analysis is needed to understand why they affect the reflectance calculation for tree regions.

The proposed method is developed and tested on a forest/grassland area in Kansas which is dominated by tall grass and is expected to show small variations in reflectance values with changes in spatial resolution. This is further validated by comparing high-resolution and resampled medium-resolution NIS SR images.

It is worth mentioning that the proposed method can be implemented using any UAS camera and satellite, including, Sentinel, Planet, etc. Also, the NIS images are used in this paper as a validation tool and is not required to implement the SCC method. In fact, this method showed its effectiveness in generating UAS reflectance image at 1 m, only because the available images for validation are at that resolution. It can potentially be applied to UAS images at higher resolutions (< 0.1 m) also.

Lastly, the proposed method has the following constraints based on the current study: 1) requirement of atmospherically-corrected satellite reflectance data which can be used as a reference for the UAS survey. Note that airborne reflectance data such as NAIP or NEON can also be used when satellite data is not available, 2) the accuracy of the reference data and their acquisition time will have an impact on the calculated UAS reflectance, and 3) the effectiveness of this method has been demonstrated in a grassland/forest field and further investigations are required to evaluate its performance in more complex landscapes and other land cover areas such as crop fields.

## 6. Conclusion

In this paper, a low-cost and novel SCC method is proposed for reflectance estimation of raw UAS DN images. This method only utilizes publicly available data without using ground calibration targets or expensive spectroradiometers, which makes it highly feasible for many UAS end-users. The proposed method showed its effectiveness through a forest/grassland area, comprising of images from a low-cost KHawk 2 UAS, L8 satellite, and NEON aircraft data. The estimated KHawk UAS NIR and Red reflectance images are validated by comparing with NIS SR images at high-resolution. High similarities are observed with reflectance differences less than 0.0137 and 0.01 for the grass regions and 0.0497 and 0.0251 for the tree regions.

Future objectives include: 1) testing the effectiveness of the proposed method with more complex landscapes and other land cover types using ground spectroscopy measurements for validation; 2) development of machine-learning based algorithms for the mapping from UAS raw DN to reflectance and validation in different types of landscapes; 3) investigating the effect of BRDF correction on UAS reflectance estimation; 4) comprehensive evaluation of this method on multiple data sets from different satellites such as Sentinel 2 and Planet.

# References

Aboutalebi, M., Torres-Rua, A.F., Kustas, W.P., Nieto, H., Coopmans, C., McKee, M., 2019. Assessment of different methods for shadow detection in high-resolution optical imagery and evaluation of shadow impact on calculation of NDVI, and evapotranspiration. Irrigation Science 37, 407–429.

ArcGIS, 2021. World imagery. URL: `https://www.arcgis.com/home/item`.

Badawi, M., Helder, D., Leigh, L., Jing, X., 2019. Methods for earth-observing satellite surface reflectance validation. Remote Sensing 11, 1543.

Barry, P.S., Mendenhall, J., Jarecke, P., Folkman, M., Pearlman, J., Markham, B., 2002. EO-1 hyperion hyperspectral aggregation and comparison with EO-1 advanced land imager and landsat 7 ETM+, in: IEEE International Geoscience and Remote Sensing Symposium, pp. 1648–1651.

Berra, E.F., Gaulton, R., Barr, S., 2017. Commercial off-the-shelf digital cameras on unmanned aerial vehicles for multitemporal monitoring of vegetation reflectance and NDVI. IEEE Transactions on Geoscience and Remote sensing 55, 4878–4886.

Deng, L., et al., 2018. A subband radiometric calibration method for UAV-based multispectral remote sensing. IEEE Journal of Selected Topics in Applied Earth Observations and Remote Sensing 11, 2869–2880.

Edwards, J., Anderson, J., Shuart, W., Woolard, J., 2019. An evaluation of reflectance calibration methods for uav spectral imagery. Photogrammetric Engineering & Remote Sensing 85, 221–230.

Foster, B.L., et al., 2010. Integrated responses of grassland biodiversity and ecosystem properties to hay management: a field experiment. Transactions of the Kansas Academy of Science 113, 103–120.

Fraser, R.H., Van der Sluijs, J., Hall, R.J., 2017. Calibrating satellite-based indices of burn severity from UAV-derived metrics of a burned boreal forest in NWT, Canada. Remote Sensing 9, 279.

Goetz, S., 1997. Multi-sensor analysis of NDVI, surface temperature and biophysical variables at a mixed grassland site. International Journal of Remote Sensing 18, 71–94.

Gowravaram, S., Tian, P., Flanagan, H., Goyer, J., Chao, H., 2018. UAS-based multispectral remote sensing and NDVI calculation for post disaster assessment, in: 2018 International Conference on Unmanned Aircraft Systems (ICUAS), pp. 684–691.

Hassan-Esfahani, L., Ebtehaj, A., Torres-Rua, A., McKee, M., 2017. Spatial scale gap filling using an unmanned aerial system: A statistical downscaling method for applications in precision agriculture. Sensors 17, 2106.

Jarecke, P., Barry, P., Pearlman, J., Markham, B., 2001. Aggregation of hyperion hyperspectral spectral bands into landsat ETM+ spectral bands, in: IGARSS 2001. Scanning the Present and Resolving the Future. Proceedings. IEEE 2001 International Geoscience and Remote Sensing Symposium, pp. 2822–2824.

Joan-Cristian, P., Munoz, F.J., Planas, J., Pons, X., 2019. Comparison of four UAV georeferencing methods for environmental monitoring purposes focusing on the combined use with airborne and satellite remote sensing platforms. International Journal of Applied Earth Observation and Geoinformation 75, 130–140.

KBS, 2019. Kansas biological survey. URL: `https://biosurvey.ku.edu/field-station`.

Liu, Y., et al., 2017. Using data from Landsat, MODIS, VIIRS and phenocams to monitor the phenology of california oak/grass savanna and open grassland across spatial scales. Agricultural and Forest Meteorology 237, 311–325.

Matese, A., et al., 2015. Intercomparison of UAV, aircraft and satellite remote sensing platforms for precision viticulture. Remote Sensing 7, 2971–2990.

Mathworks, 2020. Least-squares fitting. URL: `https://www.mathworks.com/help/curvefit/.html`.

MATLAB, 2020. Register images with projection distortion using control points. URL: `mathworks.com/help/images/registering-an-aerial-photo-to-an-orthophoto.html`.

Merino, L., Caballero, F., Martínez-De-Dios, J.R., Maza, I., Ollero, A., 2012. An unmanned aircraft system for automatic forest fire monitoring and measurement. Journal of Intelligent & Robotic Systems 65, 533–548.

Meyer, D.J., Chander, G., 2007. The effect of variations in relative spectral response on the retrieval of land surface parameters from multiple sources of remotely sensed imagery, in: IEEE International Geoscience and Remote Sensing Symposium, pp. 5150–5153.

Murugan, D., Garg, A., Singh, D., 2017. Development of an adaptive approach for precision agriculture monitoring with drone and satellite data. IEEE Journal of Selected Topics in Applied Earth Observations and Remote Sensing 10, 5322–5328.

NASA, 2019. Nasa's earth observing system. URL: `https://eospso.nasa.gov/missions/landsat-8`.

NASA, 2020. Landsat8 spectral band viewer. URL: `https://landsat.usgs.gov/spectral-characteristics-viewer`.

NASA, 2021. Landsat science. URL: `https://landsat.gsfc.nasa.gov/landsat-8/landsat-8-overview`.

Nencini, F., Capobianco, L., Garzelli, A., 2008. Weighted least squares pan-sharpening of very high resolution multi-spectral images, in: IGARSS 2008-2008 IEEE International Geoscience and Remote Sensing Symposium, pp. V–65.

NEON, 2019. Airborne remote sensing. URL: `https://www.neonscience.org/`.

NEON, 2020. About hyperspectral remote sensing data. URL: `https://www.neonscience.org/hyper-spec-intro`.

Niu, H., Zhao, T., Wang, D., Chen, Y., 2019. Evapotranspiration estimation with UAVs in agriculture: A review .

Ononye, A.E., Vodacek, A., Saber, E., 2007. Automated extraction of fire line parameters from multispectral infrared images. Remote Sensing of Environment 108, 179–188.

PeauProductions, 2017. Peaupro82 camera. URL: `https://www.peauproductions.com/products/peaupro82`.

Shimabukuro, Y.E., Smith, J.A., 1991. The least-squares mixing models to generate fraction images derived from remote sensing multispectral data. IEEE Transactions on Geoscience and Remote sensing 29, 16–20.

Stark, B., Zhao, T., Chen, Y., 2016. An analysis of the effect of the bidirectional reflectance distribution function on remote sensing imagery accuracy from small unmanned aircraft systems, in: 2016 International Conference on Unmanned Aircraft Systems (ICUAS), pp. 1342–1350.

StatisticsSolutions, 2020. Homoscedasticity. URL: `https://www.statisticssolutions.com/homoscedasticity`.

Stow, D., Petersen, A., Rogan, J., Franklin, J., 2007. Mapping burn severity of mediterranean-type vegetation using satellite multispectral data. Giscience & Remote Sensing 44, 1–23.

Teillet, P., Staenz, K., William, D., 1997. Effects of spectral, spatial, and radiometric characteristics on remote sensing vegetation indices of forested regions. Remote Sensing of Environment 61, 139–149.

Torres-Rua, A., Arab, M.A., Hassan-Esfahani, L., Jensen, A., McKee, M., 2015. Development of unmanned aerial systems for use in precision agriculture: The aggieair experience, in: 2015 IEEE Conference on Technologies for Sustainability (SusTech), pp. 77–82.

Tuominen, S., Pekkarinen, A., 2004. Local radiometric correction of digital aerial photographs for multi source forest inventory. Remote Sensing of Environment 89, 72–82.

USGS, 2020. Landsat 8 collection 1 land surface reflectance code product guide. URL: `https://www.usgs.gov/media/files/`.

Voigt, S., et al., 2007. Satellite image analysis for disaster and crisis-management support. IEEE Transactions on Geoscience and Remote Sensing 45, 1520–1528.

Wagner, M., et al., 2019. Unpiloted aerial systems (UASs) application for tornado damage surveys: Benefits and procedures. Bulletin of the American Meteorological Society .

Wang, C., Myint, S.W., 2015. A simplified empirical line method of radiometric calibration for small unmanned aircraft systems-based remote sensing. IEEE Journal of Selected Topics in Applied Earth Observations and Remote Sensing 8, 1876–1885.

Wang, Y., Ryu, D., Park, S., Fuentes, S., O'Connell, M., 2017. Upscaling UAV-borne high-resolution vegetation index to satellite resolutions over a vineyard, in: 2nd International Congress on Modelling and Simulation, Hobart, Tasmania, Australia.

Zaman, B., Jensen, A., Clemens, S.R., McKee, M., 2014. Retrieval of spectral reflectance of high resolution multispectral imagery acquired with an autonomous unmanned aerial vehicle. Photogrammetric Engineering & Remote Sensing 80, 1139–1150.

Zhang, L., Yang, L., Lin, H., Liao, M., 2008. Automatic relative radiometric normalization using iteratively weighted least square regression. International Journal of Remote Sensing 29, 459–470.

Zhao, H., Jia, G., Li, N., 2010. Transformation from hyperspectral radiance data to data of other sensors based on spectral superresolution. IEEE Transactions on Geoscience and Remote Sensing 48, 3903–3912.

Zhao, T., Stark, B., Chen, Y., Ray, A.L., Doll, D., 2015. A detailed field study of direct correlations between ground truth crop water stress and normalized difference vegetation index (NDVI) from small unmanned aerial system (sUASs), in: 2015 International Conference on Unmanned Aircraft Systems (ICUAS), pp. 520–525.